Flow and heat transfer around a diamond-shaped cylinder at moderate Reynolds number

Arkadii Sochinskii, Damien Colombet, Manuel Medrano Muñoz, Frédéric Ayela, Nicolas Luchier

Flow and heat transfer around a diamond-shaped cylinder at moderate Reynolds number

A. Sochinskii[a,b], D. Colombet[a,*], M. Medrano Muñoz[b], F. Ayela[a], N. Luchier[b,c],

[a] *Univ. Grenoble Alpes, CNRS, Grenoble INP, LEGI, 38000 Grenoble, France*
[b] *INAC-SBT, Grenoble, France*
[c] *CEA, Grenoble, France*

Abstract

Hydrodynamics and heat transfer around a diamond-shaped cylinder in a stationary flow have been investigated using direct numerical simulation. Simulations were carried out for a steady flow with a Reynolds numbers ranging from 1 to 70 and for a Prandtl number corresponding to a gas ($Pr = 0.7$). The study focuses on the influence of the diamond apex angle α ($33 \leq \alpha \leq 120°$) on the evolution of drag, wake length and Nusselt number. A comparison with the case of a circular cylinder is performed. It is shown that the drag coefficient of a diamond-shaped cylinder remains very close to the one of a circular cylinder ($\pm 10\%$) for $Re < 10$ and that it is reduced by decreasing the apex angle for $Re > 10$. In the same time, compared to the circular cylinder case, the reduction of the apex angle postpones significantly the Reynolds corresponding to the wake recirculation onset. When the Reynolds reference velocity is, as often, taken as the far field velocity, the corresponding Nusselt numbers are found to decrease with the apex angle α. However, it is found that when the reference velocity is based on the maximal vorticity near the equator, the Nusselt number of diamond-shaped cylinders seems to collapse on a single master curve. This may indicate that the relevant velocity scale to describe Nusselt variation, and thus the heat transfer, is dependant on the interfacial vorticity intensity rather than on the far field velocity.

Keywords:
Diamond-shaped cylinder, Fluid mechanics, Heat transfer

*damien.colombet@univ-grenoble-alpes.fr

1. Introduction

Arrays of diamond-shaped cylinders are often employed to design compact heat exchanger. Heat transfer and pressure drop were characterised by Chyu et al. [1], Tanda [2] or Jeng [3] for in-line or staggered matrix of square or diamond-shaped cylinders. Chyu et al. [1] found experimentally that staggered matrix of square cylinder arrays deliver higher transfer rate than diamond-shaped cylinder arrays followed by circular cylinder arrays. The transfer was studied using a naphthalen sublimation technique. Tanda [2] have quantified the transfer and the temperature distribution in a flow through different cylinder arrays using liquid crystal thermography. According to the authors, for a given mass flow rate, a diamond-shaped cylinder array is up to 4.4 more efficient than an empty channel. The heat transfer efficiency was also investigated experimentally by Jeng [3] for the case of an in-line array of diamond-shaped cylinders using a transient method for measuring the heat transfer coefficient. The authors have concluded that for a given pumping power it is possible to found an optimal distance between cylinders to maximize heat transfer. One can notice that square cylinders matrix geometry was also employed to investigate accurately roughness effect on laminar flow [4].

In the literature, it is important to emphasize that diamond-shaped cylinder arrays are usually rotated square-shaped cylinders (i.e. diamond shape with an apex angle of $\alpha = 90°$). The effect of varying the apex angle (or cylinder section aspect ratio) is not systematically performed.

The design of a heat exchanger with such a geometry in a staggered arrangement was used in space industry for electronic cooling applications. The pressure drop coefficient in such geometries were characterised experimentally and numerically by Sparrow & Grannis [5] for an apex angle of 45 and $90°$ with a Reynolds number range of $20 < Re < 2700$ in order to give correlations to assist sizing of an air/air heat exchanger for a space shuttle. Later, an array of diamond-shaped cylinders was also investigated by Vanapalli et al. [6] for cryocooling of the electronic employed in satellite. For a laminar flow at moderate Reynolds numbers ($50 \leq Re \leq 500$) and an apex angle of $\alpha = 37.15°$, Vanapalli et al. [6] found experimentally that a diamond-shaped cylinder matrix generates higher pressure drop than circular, square, elliptical or sinus shape. In microfluidics, the diamond-shaped cylinder arrays were also investigated for liquid phase chromatography applications [7, 8].

For a turbulent flow regime, to better understand the control of multiple jets formation device, the jets formation with a specific flapping instability has been studied at the outlet of a liquid flow discharging directly into air past an array of diamond-shaped cylinders [9, 10]. For such a flow, funded on numerical simulation and experimental measurements, Hirasawa et al. [11] proposed correlations to describe the pressure drop and the heat transfer in an array of diamond-shaped cylinders with an apex angle of $\alpha = 30°$. At last, porous diamond-shaped cylinders had a particular interest for biological filtering processes [12, 13, 14, 15]. At moderate Reynolds number,Rashidi et al. [12] and Vijaybabu et al. [15] have characterised heat transfer and Nusselt number for the flow around a solid diamond-shaped cylinder of apex angle $\alpha = 90°$. The influence of the apex angle on the flow around a porous diamond-shaped cylinder was studied by Rashidi et al. [13]. As a result, the knowledge of the flow and heat transfer around a single diamond-shaped cylinder may be benefit for various applications.

While the literature on single circular or square cylinder geometry is large (see for example [16, 17, 18, 19, 20, 21, 22, 23, 24, 25, 26, 27, 28]), very few studies deal with the flow and/or the mass transfer around a single diamond-shaped cylinder. Yoon et al. [29] performed a numerical study to understand the key parameters for the description of a laminar flow around an inclined

single diamond-shaped cylinder having an apex angle of $\alpha = 90°$ with different angle of incidence ($Re \leq 150$). In this article, the influence of the incident angle on the flow pattern, the drag and lift, the angle of separation and the Strouhal number (linked to vortex shading frequency in the cylinder wake) is analysed. The flow around a single diamond-shaped cylinder confined in a channel has been studied by Djeddi et al. [30] using direct numerical simulation for low and moderate Reynolds numbers ($Re < 200$). In this work, the Strouhal number variation was characterized against the cylinder aspect ratio and a blockage coefficient. Numerical simulation of the flow around a square and diamond-shaped cylinder with an apex angle of $90°$ for larger Reynolds number ($Re = 250 - 1000$) have been presented by Dalton & Zheng [31]. The authors found that for such Reynolds number range, rounding the corner of square or diamond-shaped cylinders affected significantly the lift and drag coefficients. The flow and the heat transfer through and around a porous diamond-shaped cylinder in a laminar flow has been investigated by Rashidi et al. [12, 13]. In these works, it is shown that the variation of the apex angle and cylinder internal porosity influenced the drag and the critical Reynolds number corresponding to wake recirculation onset. A numerical study of heat transfer in a cross flow for streamlined cylinders was performed by Li et al. [32]. The cylinders shapes were elliptical and lenticular with minor-to-major axis ratios of 0.3, 0.5 and 0.8. The authors results suggest that for the Reynolds range $500 \leq Re \leq 10^4$, the drag coefficient of tubes could be reduced by 30-40 % with just 15-35 % losses on the averaged Nusselt number compared with the circular cylinder case.

Concerning experimental data available in the literature, the measurements of the drag coefficients of various single cylinders with different cross sectional shapes published by Delany & Sorensen [33] can be mentioned. The drag coefficients were obtained for cylinders of elliptic, rectangular, diamond or triangle shapes for various aspect ratio 0.5, 1, 2 ($\alpha = 53$, 90, $126°$) and corners radius (smoothed corners) at large Reynolds numbers ($1 \times 10^4 \leq Re \leq 2 \times 10^6$).

To authors knowledge, even if there is already different applications employing such a geometry, the literature on the analysis of the flow and heat transfer around a single diamond-shaped cylinder remains very limited. The objective of the present study is to investigate diamond-shaped cylinder hydrodynamics and heat transfer for $1 \leq Re \leq 70$ in a steady flow (no wake oscillation nor vortex shading). For this purpose, numerical simulations of the laminar flow around a cylinder are first performed to establish the drag coefficient and the recirculation length for an apex angle varying in the range $\alpha = 33 - 120°$. Then, heat transfer simulations are conducted for $Pr = 0.7$ to understand the influence of the apex angle on the heat flux and on the Nusselt number. Finally, the effect of the variation of interfacial vorticity on heat transfer is also investigated.

The paper is organized as follows. Sections 2 and 3 present the governing equations and the numerical procedure, respectively. Section 4 is devoted to the validation of the numerical procedure for both the fluid flow and the transfer by comparison with the circular cylinder case that is well documented in the literature. Section 5 presents and discusses the numerical results in order to improve the modelling of the steady flow and heat transfer from diamond-shaped cylinders.

2. Governing equations

In this section, the main equations used for this study are presented. The numerical simulation of the flow and the heat transfer is considered for the case of a cylinder with a constant far field velocity 'U'. The cylinder length aspect ratio is considered to be small enough so that the flow is in two dimensions (i.e. $a/H << 1$). Due to the Reynolds range, the flow regime is laminar. The

local velocity vector '$\mathbf{u}$' and pressure 'p' fields are given by solving numerically the Navier-Stokes equations for an incompressible Newtonian fluid

$$\nabla \cdot \mathbf{u} = 0 \tag{1}$$

$$\rho \mathbf{u} \cdot \nabla \mathbf{u} = -\nabla p + \nabla \cdot \overline{\overline{\tau}} \tag{2}$$

where $\overline{\overline{\tau}} = \mu \left(\nabla \mathbf{u} + \nabla^T \mathbf{u} \right)$ is the viscous contribution of the stress tensor, ρ and μ are respectively the fluid density and the dynamic viscosity. Far from the cylinder, the fluid satisfies the condition $\mathbf{u} \rightarrow U\mathbf{e_x}$. Note that the use of the Navier-Stokes equations without temporal terms is only possible because the flow remains steady and non oscillatory for present geometries and Reynolds range.

The unsteady advection-diffusion equation is solved for the temperature around the cylinder

$$\frac{\partial T}{\partial t} + \nabla \cdot (T\,\mathbf{u}) = D_T \nabla^2 T \tag{3}$$

with T the local temperature in the flow, $D_T = \lambda/(\rho C_p)$ the heat diffusivity coefficient where C_p and λ are respectively the heat capacity at constant pressure and the thermal conductivity of the fluid. The use of the unsteady formulation of the enthalpy conservation equation (Eq. 3) was initially done to enable the study of heat transfer in transient condition. But this topic was finally out of the scope of the present work.

The heat transfer is investigated varying the Reynolds number of the flow that is calculated as

$$Re = \frac{\rho\, U\, L_{ref}}{\mu} \tag{4}$$

where L_{ref} is the cross length of the cylinder perpendicular to the main flow: for a circular cylinder it corresponds to its diameter $L_{ref} = D$, for a diamond-shaped cylinder it corresponds to its width $L_{ref} = a$. The flow around the cylinder is mainly characterized by the corresponding drag coefficient and by the length of the recirculation formed in the cylinder wake. The drag coefficient is calculated, from the calculation of the drag force $\mathbf{F_d}$ by integrating the pressure and viscous stress on the surface of the cylinder

$$C_D = \frac{1}{A_p (1/2) \rho U^2} \, ||\mathbf{F_d}|| = \frac{1}{A_p (1/2) \rho U^2} \left|\left| \int_S (-p \cdot \mathbf{n} + \overline{\overline{\tau}} \cdot \mathbf{n}) dS \right|\right| \tag{5}$$

with $\mathbf{n}$ the normal surface unit vector. A_p corresponds to the projected surface area based on the product of the cylinder width with its length ($D \times H$ or $a \times H$). In present flow conditions, the global resulting force experienced by the column is only the drag force $\mathbf{F_d}$, along the $\mathbf{e_x}$ axis, because the lift force is zero since the inlet velocity is constant and the column's shape is symetric.

In this work, the heat transfer around the cylinder is characterized using the surface averaged Nusselt number as

$$Nu = \frac{J}{\lambda (T_p - T_\infty)/L_{ref}} = \frac{h L_{ref}}{\lambda} \qquad \text{with} \quad J = \frac{1}{S} \int_S J_{loc} dS \tag{6}$$

with J the surface averaged heat flux, ~~$J_{loc} = -\lambda(\partial T/\partial \mathbf{n})$~~ $J_{loc} = -\lambda(\partial T/\partial n)$ is the local heat flux at the cylinder surface. S stands for the cylinder surface. T_p and T_∞ are respectively the temperature imposed at the solid/gas interface (i.e. the cylinder wall) and the temperature of the flow far from the cylinder. h is the corresponding heat transfer coefficient in $\mathrm{W\,m^{-2}K^{-1}}$.

3. Numerical procedure

The conservation equations are solved with the finite volume method in 2D with OpenFoam using a double-precision writing format [34]. Navier-Stokes equations are first solved to obtain the steady pressure and velocity fields around the cylinder for a given Reynolds number (Eq. 1-1). Then, using the resulting velocity field, the advection-diffusion equation is solved for $Pr = \nu/D = 0.7$ to get the temperature field (Eq. 3).

In order to solve the Navier-Stokes equations, an upwind second order scheme and a centred second order scheme are used for the spatial discretisation of respectively the advective and the diffusive fluxes. The pressure and velocity fields are linked by the SIMPLE algorithm. The convergence of the flow calculation is achieved when the drag coefficient is stable and the residuals are lower than 10^{-7}.

In order to solve the enthalpy conservation equation, convective flux are calculated using a TVD second order scheme with a Sweby limiter, while diffusive fluxes are discretized with a centred second order scheme as for the momentum equation. The transient term is then discretized with a second order scheme and the equation is solved with an implicit method. The convergence of the flow calculation is achieved when the Nusselt number stabilizes.

The diamond shape geometry and the corresponding dimension parameters are presented in Fig. 1. The calculation domain is presented in Fig. 2. For both circular and diamond-shaped cylinders, a constant velocity U and a zero normal pressure gradient are imposed at the inlet of the domain. A constant pressure reference p_0 and a zero normal velocity gradient are imposed at the domain outlet. An adherence condition is imposed at the cylinder wall ($\mathbf{u} = \mathbf{0}$). A symmetry boundary condition is set on the main axis. For heat transfer simulation a constant temperature T_p is imposed at the walls. A constant temperature T_∞ is set at the inlet, while a zero normal temperature gradient is chosen as the boundary condition for the outlet. The temperature and the velocity are initially set to $T = T_\infty$ and $\mathbf{u} = U\mathbf{e_x}$ in the whole calculation domain.

An example of the grid employed in this work is shown in Fig. 3. Around the cylinder a body fitted rectangular mesh is used. In order to limit the boundary effects, the domain size is chosen to be $R_\infty/R = 60$ for the circular cylinder case and $L_A/a = L_B/a = 60$ with $L_D/a \geq 60$ for the diamond shape case. This limit is known to be high enough for limiting the influence of the domain border for the simulation of 3D spherical objects for $1 \leq Re \leq 300$ [35]. This value has been also employed by Rashidi et al. [13] for 2D simulations of a diamond-shaped cylinder for $2 \leq Re \leq 46$. For the circular cylinder, the number of cells along the wall is $N_\theta = 100$. Such value is found to be convenient for 2D simulation of the flow around a circular cylinder [23] or around a spherical object [36, 37]. For the diamond shape, two construction lines are added and attached to the front and back apex angle in order to control the cells deformation near the wall.

In the present simulations, since the Reynolds and the Peclet number $Pe = Pr \times Re$ remain low, the dynamic and thermal boundary layers around the object are thick. Thus the smallest size of the cell at the cylinder surface is not fixed by a boundary layer constraint but by respecting a cell aspect ratio between 2 and 4 and checking the grid refinement independence. The detail on

computational domain and grid sizes for diamond-shaped cylinder case is given Table 1. Total cell numbers are indicated in the last column. In addition, with a Prandtl number of $Pr = 0.7$, the thermal boundary layer δ_T is expected to be weakly larger than the dynamic boundary layer of the flow around the cylinder δ_ν. As a result, in contrast with the cases where $Pr >> 1$, the same grid which is optimized for the flow simulation can be used for the simulation of heat transfer.

The result independence on the grid sizes has been tested for each cases and the data obtained for $\alpha = 33$ and $90°$ with respectively $Re = 100$ and 40 are presented here. Table 2 presents the values of the drag coefficient and the Nusselt number for four different meshes A, B, C, D. In this table, the relative difference is also reported. When decreasing the cell size, the results are found to converge with a relative difference lower than 1.5% compared to grid B. The grid used for the following simulations is thus chosen as grid B. As shown in Table 2 it is shown that a more refined mesh (ex: mesh (A)) does not change the resulting convergence.

4. Preliminary validation with the circular cylinder geometry

In this section, some preliminary validations for the resolution of both the Navier-Stokes equations and the temperature equation are reported for the case of a circular cylinder.

4.1. Vorticity and drag coefficient

In order to get the validation of the resolution of the Navier-Stokes equations, the vorticity at the circular cylinder surface has been compared to the one reported by Dennis & Chang [20]. In a 2D flow, the vorticity vector ~~is simply~~ has only one component on the $\mathbf{e_z}$ axis as following

$$\Omega = (\nabla \times \mathbf{u}) \cdot \mathbf{e_z} = \frac{\partial u_y}{\partial x} - \frac{\partial u_x}{\partial y} \tag{7}$$

For $Re = 5$, 7, 10, 20 and 40, the distribution of the vorticity along the cylinder surface is plotted in Fig. 4 against its angular position θ (for the definition of the angular position see Fig. 1). Since the vorticity corresponds to the fluid particle rotation intensity, when no recirculation occurs for $Re \leq 7$, only positive values are found. In agreement with Dennis & Chang [20], for $Re > 7$, the vorticity can be negative for $\theta > 110°$ because of the formation of a recirculation behind the circular cylinder that appears around $Re_{crit} \approx 6.24$. Fig. 4 clearly shows that present numerical results are in very good agreement with the work of Dennis & Chang [20]. Then, to check the validity of the procedure used for the calculation of the drag coefficient, the results are compared with previous numerical works. The comparison is presented in Table 3. The difference between the drag coefficients obtained in this work and the drag coefficients found by Dennis & Chang [20], Fornberg [21] and Kalita & Ray [23] is lower than 2%. In addition, for $Re < 10$, a very good agreement is found with the correlation proposed by Sheard et al. [22]

$$C_D = 11.09\, Re^{-0.61} \tag{8}$$

As shown in Tab. 3, where the numerical results obtained by Sheard et al. are also reported, for $Re = 1$, the relative difference on the drag with present numerical simulation is only of 4%. As a result, the limitation of the transverse size of the calculation domain to $R_\infty/R = L_A/a = L_B/a = 60$ seems to be enough to neglect the effect of the lateral boundary on numerical results for $Re \geq 1$. This work remains also in agreement with the measurements performed by Tritton [18].

4.2. Heat transfer

An example of the velocity field and the corresponding temperature field for the heat transfer around a circular cylinder is presented in Fig. 5a for $Re = 1$ and $Re = 40$. As expected, at low Reynolds numbers, the thermal boundary remains thick and quite homogeneous around the cylinder. At higher Reynolds number, due to the enhancement of the advection the thermal boundary layer is much thinner around the cylinder and especially at the front part. Because of the formation of the recirculation behind the cylinder, heat is trapped in the wake so that most of the heat transfer takes place on the front part of the cylinder where the temperature surface normal gradients are the highest. For the circular cylinder case, Nusselt numbers obtained from numerical simulations and from some previous experimental works are reported in Table 3. Present results verify the correlation proposed by Collis & Williams [19] which is valid for $Pr = 0.7$ and $0.02 < Re < 44$

$$Nu = 0.24 + 0.56\, Re^{0.45} \tag{9}$$

The maximal difference with this correlation is lower than 2.3%. Nusselt values given by Hilpert [16] are found to be systematically $4 - 9\%$ higher. While the difference with predicted values found by Mc Adams[17] is larger than $3-8\%$ for $Re < 30$ and lower than 2% for $Re \geq 30$. The analysis of the variation of the vorticity surface distribution, of the drag coefficient and of the Nusselt number for different Reynolds number for the circular cylinder geometry has enabled us to validate the numerical simulation procedure of the flow and of the heat transfer around a cylinder.

5. Results and discussion

This section presents and discuss the results obtained for the flow and the heat transfer for the case of a diamond-shaped cylinder with an apex angle in the range $33 \leq \alpha \leq 120°$ for a Reynolds number range of $1 \leq Re \leq 70$.

5.1. Wake length, vorticity and drag coefficient

Some examples of velocity fields and streamlines for the case of the flow around a diamond-shaped cylinder are given in Fig. 5b-e for $\alpha = 33 - 60 - 90 - 120°$ for $Re = 1$ and $Re = 40$. As reported in the top part of those figures, when the Reynolds increases, as for the circular shape, a recirculation can appear in the wake of the pillar. An estimation of the critical Reynolds number Re_{crit} corresponding to the onset of the recirculation is given in Table 4. It can be noticed that the critical Reynolds number for a diamond shape with $\alpha = 90°$ (inclined square, $Re_{crit} = 7.4$) is very close to the one of the circular cylinder case ($Re_{crit} = 6.24$). Then if the apex angle decreases, for $\alpha < 90°$, the recirculation onset can be significantly postponed. For example, one needs to reach $Re_{crit} = 55$ to begin to get a recirculation for $\alpha = 30°$. On the contrary if the apex angle increases, for $\alpha > 90°$, the recirculation appears at lower Reynolds numbers than with a circular cylinder (i.e. $Re_{crit}(\alpha > 90°) < Re_{crit}$(circular cylinder)).

The recirculation wake length has been plotted in Fig. 6 as a function of the Reynolds number (symbols). It is defined in this work as the distance between the back extremity of the diamond shape till the position where the sign of the velocity component along the x-axis is changed (see Fig. 1). As shown in Fig. 6, similarly to the circular cylinder case, the variation of the dimensionless wake length for a diamond-shaped cylinder evolves linearly with the Reynolds number following relation here after, for $Re > Re_{crit}$

$$\frac{L}{(a/2)} = A\,Re + B \tag{10}$$

with the constants A and B given in Table 4. The values obtained for a circular cylinder from numerical simulations are also reported in Table 4. For a circular cylinder, as reported in Fig. 6, the maximal difference between Eq. 10 and numerical simulations of Kalita & Ray [23] is about $5-6\%$. Fig. 6 enables to show that for a given Reynolds number the dimensionless wake length increases with the apex angle. Thus, one can conclude that the decrease of the apex angle can prevent the formation of a recirculation behind diamond-shaped cylinder and decrease its relative length ($L/(a/2)$). This behaviour is found to be in agreement with previous results of Rashidi et al. [13] for the case of a porous diamond-shaped cylinder. In addition, it is interesting to note that the delay of the onset of the recirculation formation has also the effect to postpone the critical Reynolds number corresponding to the onset of the unsteady oscillatory flow. For a circular cylinder it is well known that the flow becomes unsteady for a Reynolds number between 40 and 50. For deformed cylinder where the length is longer in the streamwise direction than in the transverse direction, it have been already shown that the deformation postpone significantly the onset of the oscillatory flow. For example for a deformed elliptic cylinder with an aspect ratio of $b/a = 2$ corresponding here to an apex angle of $\alpha \approx 50^\circ$ with the diamond-shaped geometry, the critical Reynolds number for the onset of the unsteady flow is near to 75 [38, 39]. Even if the stability analysis of a flow around a diamond-shaped cylinder is out of the scope of the present work, some preliminary numerical tests with transient simulations have confirmed that the oscillatory flow regime onset Reynlods number is larger than the Reynolds range investigated in this work. The corresponding data are reported in the last column of Table 4.

In order to understand the formation of the recirculation and to compare with the circular cylinder case, for $Re = 1,\ 10,\ 40$ and $\alpha = 33,\ 60,\ 90,\ 120^\circ$, the vorticity profiles have been plot in Fig. 7 as a function of the angular position θ. Globally, for all the cases one can observe that the vorticity distribution over a diamond shape is less homogeneous than on a circular shape and present up to three local maxima at the two apex angles ($\theta = 0$ and $\theta = 180^\circ$) and near the equator angle. This last result induces that the separation angle (where the tangential velocity change of sign along the cylinder surface) is almost always close to $\theta \approx 90^\circ$ for diamond shape while it depends on the Reynolds number for circular shape. For $Re = 1$, Fig. 7a shows that, as for the circular shape, the vorticity on diamond shape remains positive because no recirculation occurs. In Fig. 7b and c, because of the formation of the recirculation the vorticity of the diamond shape is negative at the back (for $\theta > 90^\circ$) at $Re = 10$ for $\alpha = 90 - 120^\circ$ and at $Re = 40$ for $\alpha = 60 - 90 - 120^\circ$.

In Fig.8, the evolution of the maximal vorticity intensity obtained for the peak near the equator ($\theta \approx 90^\circ$) is plotted as a function of Re. As shown in this figure, it is interesting to notice that the variation of this value is found to increase with the Reynolds number and can be described by the following power law

$$\Omega_{max} = A\,Re^n \tag{11}$$

with $0.8 < A < 3$ and $0.4 < n < 0.5$ as reported in Table 5.

The drag coefficient of a diamond-shaped cylinder is now compared to previous works. The drag coefficient of a diamond-shaped cylinder with $\alpha = 90^\circ$ (square cylinder inclined at 45°) is first plotted as a function of the Reynolds number in Fig. 9. In this figure, the results obtained by Yoon

et al. [29] are also reported (the sum of the pressure and viscous contribution presented in Fig. 19 in the article). As reported in this figure, numerical results are in good agreement with the data reported by Yoon et al. [29]. In this figure, the results obtained for the circular cylinder case is also plotted. This comparison shows us that the drag coefficient of a $90°$ apex angle diamond shaped cylinder is in fact very close to the one of a circular cylinder meaning that those two geometries experience a similar drag force intensity.

Secondly, the drag coefficient of all the diamond-shaped cylinders considered and of the circular cylinder are plotted in Fig. 10 for $1 \leq Re \leq 10$ (a) and $10 \leq Re \leq 70$ (b). Globally, for Reynolds number lower than 10, one can observe that the drag coefficients obtained for a large range of apex angle ($33 \leq \alpha \leq 120$) remain close to the one expected for a circular cylinder. As shown in Fig. 10a the drag differs from less than 10% from the circular cylinder drag law for $Re < 10$. Therefore, for that Reynolds number range, the use of a reference length corresponding to the projected area of the cylinder perpendicularly to the main flow direction ($L_{ref} = a$) enables almost to apply a quasi similitude with the circular cylinder case.

A detailed analysis of present results shows that at low Reynolds number ($Re = O(1)$) the decrease of the apex angle still generates an increase of the drag coefficient. For a given cylinder width 'a', this behaviour is due to the enhancement of the friction since when the apex angle decreases the length 'b' and thus the total surface of the cylinder are larger, increasing the total wall friction.

Then, for Reynolds numbers larger than 10 and $\alpha = 120°$ (Fig. 10b) the drag is found to be higher than the circular cylinder drag law. While for Reynolds numbers larger than 20 and $\alpha < 90$, the drag is systematically lower than the circular cylinder drag law and can be reduced of more than 10%. Since for moderate Reynolds number, it is known that the drag is very sensitive to the development of the recirculation in the cylinder wake, this behaviour may results from the early (resp. late) onset of the recirculation behind diamond-shaped cylinder for $\alpha > 90$ (resp. $\alpha < 90$), as reported by Fig. 6 or Table 4.

The present results can be described by the following correlation

$$C_D = \frac{A}{Re}\left(1 + B\, Re^n\right) \tag{12}$$

with A, B and n given in Table 6. The format of this relation is chosen as the product of the drag behaviour at low Reynolds numbers (in a Stokes flow $C_D \propto 1/Re$) and a correction (in the parenthesis) that takes into account the effect of the recirculation development on the drag. Eq. 12 is able to reproduce numerical results with less than 2.5% of difference. The validity of such a relation and constant values are restricted to the present investigated Reynolds range. For lower Reynolds number ($Re << 1$) the constant 'A' may need to be adjusted.

5.2. Heat transfer

Some examples of the temperature field for the case of the steady flow around a diamond-shaped cylinder are presented in the bottom part of Fig. 5b-e for $\alpha = 33$, 60, 90, $120°$ and $Re = 1$, 40. As for the circular cylinder case, for $Re = 1$, the thermal boundary layer is thick and almost symmetric and weakly smaller at the front part than at the rear part of the cylinder because of advection effect. Then at a higher Reynolds number as $Re = 40$, this thickness difference between the front and rear boundary layer increases and recirculation can affect heat transport in the cylinder wake.

The corresponding local heat flux distributions over the cylinder surface are presented in Fig. 11 as a function of the angular position for $Re = 1$, 10, 40. As shown in this figure the surface distribution of the heat flux around a diamond-shaped cylinder is much less homogeneous than for a circular cylinder. In contrast with the circular cylinder case, the diamond-shaped cylinder case exhibits three local heat flux maxima at the front and the back apex angle ($\theta = 0, 180°$) and at the equator angle ($\theta \approx 90°$). Such a heat flux distribution with more than one local maxima has been also reported in the literature by Dhiman et al. [27], Sahu et al. [28], Dhinakaran & Ponmozhi [40] and Morenko et al. [41] for the case of heat transfer around a solid or porous square cylinder. Globally, in Fig. 11, for a given Reynolds number a decrease of the apex angle supplies lower local heat flux. For $Re = 1$, a modification of α changes both the heat flux at the front and at rear part of the cylinder. While for larger Reynolds number it can be noticed that the local heat flux is mainly changed at the front part of the cylinder ($0 \leq \theta \leq 90°$). Therefore, for large Reynolds number, the apex angle affected primarily the heat flux at the front of the cylinder.

The Nusselt numbers for diamond-shaped and circular cylinders are plotted as a function of the Reynolds number in Fig. 12. First, for the particular case of the diamond shape with $\alpha = 90°$ (inclined square cylinder), similarly to the drag coefficient, the Nusselt number is found to be close to the circular cylinder one. Moreover as reported in Fig. 12 and Tab. 7, present results are found to be in good agreement with Nusselt values obtained previously by Rashidi et al.[12] or Vijaybabu et al. [15] for data with a low porosity ($Da = 10^{-6}$) corresponding to a solid cylinder with $\alpha = 90°$.

Secondly, for a given Reynolds number, in agreement with local heat flux variations, one can observe that a decrease of the apex angle induces a reduction of the Nusselt number. Such behaviour has been also reported by Li et al. [32] for the case of heat transfer from an elliptical or lenticular cylinder at high Reynolds number. As shown in the temperature fields presented previously in Fig. 5, for a given Reynolds number, this behaviour is due to an increase of the mean thickness of the thermal boundary layer δ_T when the apex angle decreases. This is clearly shown at the equator location for $Re = 1$. Indeed, at a first order the Nusselt number corresponds to the ratio between the cylinder width and the mean thickness of the thermal boundary layer so that $Nu \approx a/\delta_T \propto Re^{1/2}$. So if the thermal boundary layer is changed due to cylinder shape modifications, the interfacial normal temperature gradient and thus heat flux and Nusselt number are affected. Globally, the evolution of the Nusselt number is found to be well represented by the following relation, for $Pr = 0.7$

$$Nu = A + B\, Re^{1/2} \tag{13}$$

where the constants A and B are given in Table 8. The format of this relation is chosen knowing that at large Reynolds number (potential flow) the Nusselt number obeys $Nu \propto Re^{1/2}$. Equation 13 enables to describe numerical results with an accuracy of 5% for $Re = 1$ and lower than 2% for $Re > 1$. It is interesting to note that contrary to the case of heat transfer around 3D objects the value of the constant A do not correspond to the analytical solution of the pure diffusion problem. Indeed, in 2D, one can show easily that there is not a universal analytical solution for the Nusselt number (see Bird et al. [42] p. 440 chap. 14).

To better understand the discrepancies observed on Nusselt number when varying the apex angle, a first attempted was to change the reference length used to calculate Re and Nu since, contrary to a circular cylinder, a diamond shape includes two length parameters (a and b). But just modifying the reference length would simply shift the Nu(Re) curves since both would be

corrected by the same length ratio (Eq. 4 and 6). Therefore, the use of an other flow reference velocity in the calculation of the Reynolds number have been investigated. In a recent work, Colombet et al. [43] have shown that to describe transfers inside or around a spherical bubble the relevant velocity scale should be the maximal velocity at the gas/liquid interface (slip condition). In addition, for a spherical bubble, Legendre [44] has demonstrated that the maximal velocity at a bubble surface is directly linked to the maximal interfacial vorticity as $U_{max} = \Omega_{max} R/2$. As a result, by choosing U_{max} as the reference velocity for Reynolds calculation, Colombet et al. [43] have in a sense calculated the reference velocity from the maximal vorticity magnitude at a bubble surface. Consequently, applying a similar approach, the following effective Reynolds number have been proposed

$$Re' = \frac{U'}{U} Re = \frac{U' a}{\nu} \tag{14}$$

where the velocity scale $U' = \Omega_{max}(a/2)$ is estimated from the maximal vorticity magnitude near the diamond shape equator (Fig. 8). The evolution of the Nusselt number as a function of the Reynolds number Re' is plotted in Fig. 13. The Nusselt number for a circular cylinder is also reported. As shown in this figure, for the diamond shape, the Nusselt number values seem to collapse on the master curve given by

$$Nu = 0.56\, {Re'}^{0.28} \tag{15}$$

This relation is able to predict present results with a maximal difference of 8% for $Re = 1$ and less than 3% for $Re > 1$. In the same time, it can be noticed that this relation does not match the Nusselt evolution of a circular cylinder. As a result, using the vorticity magnitude at the cylinder wall can allow to apply a similitude only between diamond-shaped cylinder of different aspect ratios (or apex angle). Some additional tests have been performed using the maximal vorticity at the front apex angle and the average vorticity on the cylinder surface. But the best results are obtained when the reference velocity is calculated from the maximum vorticity near the equator. Such behaviour tends to suggest that the vorticity intensity plays a key role in the transport of heat at the cylinder surface.

6. Conclusions

The flow and heat transfer around a single diamond-shaped cylinder have been studied for a laminar incompressible flow at moderate Reynolds number ($1 \leq Re \leq 70$) and a Prandtl number of $Pr = 0.7$ on a large range of apex angle $33 \leq \alpha \leq 120°$. For $Re \leq 10$, the drag coefficient of a diamond shape is found to remain close to the one of a circular cylinder. For $Re > 10$, the drag is systematically lower (resp. higher) with $\alpha < 90°$ (resp. $\alpha > 90°$) than the circular cylinder one. In agreement with the previous work of Rashidi et al. [13], it is also observed that the decrease of the apex angle increases drastically the critical Reynolds number corresponding to the onset of the wake recirculation. As for a circular cylinder, the growth of the recirculation remains proportional to the Reynolds number.

Concerning heat transfer, in agreement with previous works on heat transfer from a square cylinder, the distribution of the local heat flux is also found to present more than one local maximum and a strong variation near the equator angle. The corresponding Nusselt number versus the conventional Reynolds number is found to decrease if the apex angle is reduced. For the whole

Reynolds range the Nusselt number but also the drag coefficient of a diamond shape with $\alpha = 90°$ are almost matching the one of a circular cylinder. New correlations are proposed to describe the drag coefficient, the recirculation length and the Nusselt number variation.

In a last part, it is shown that a similitude between diamond-shaped cylinder of different apex angle ($90 \leq \theta \leq 120°$) is possible if the reference velocity for the calculation of the flow Reynolds number is based on the maximal vorticity near the equator angle of the cylinder. In this way, the Nusselt numbers collapse on a master curve that depends only on this 'effective' Reynolds number. The previous work of Colombet et al. [43] and this work may indicate that the relevant velocity scale to describe convection near the interface where transfer occurs is not the far field velocity but rather the velocity scale induced by the vorticity. This result opens new insight in the study and the description of heat or mass transfers from 2D or 3D objects. As a perspective, it would be interesting to analyse Nusselt number variations against this Reynolds number formulation for other geometries and different Prandtl numbers.

Acknowledgments

The authors would like to thank LANEF and TEC21 laboratories of excellence, SBT/CEA and LEGI for supporting this work. We also thank warmly Cyrille Bonamy for is help in numerical simulations with OpenFoam.

References

[1] M. Chyu, Y. Hsing, V. Natarajan, Convective heat transfer of cubic fin arrays in a narrow channel, Journal of Trubomachinery 120 (1998) 362–367.

[2] G. Tanda, Heat transfer and pressure drop in a rectangular channel with diamond-shaped elements, International Journal of Heat and Mass Transfer 44 (2001) 3529–3541.

[3] T. Jeng, Thermal performance of in-line diamond-shaped pin fins in a rectangular duct, International communication in heat and mass transfer 33 (2006) 1139–1146.

[4] G. Gamrat, M. Favre-Marinet, S. Le Person, R. Baviere, F. Ayela, An experimental study and modelling of roughness effects on laminar flow in microchannels, Journal of Fluid Mechanics 594 (2008) 399–423.

[5] E. Sparrow, V. Grannis, Pressure drop characteristics of heat exchangers consisting of arrays of diamond-shaped pin fins, Int. J. Heat Mass Transfer 34 (1991) 589–600.

[6] S. Vanapalli, H. Ter Brake, H. Jansen, J. Burger, H. Holland, T. Veenstra, M. Elwenspoek, Pressure drop of laminar gas flows in a microchannel containing various pillar matrices, Journal of Micromechanics and Microengineering 17 (2007) 1381–1386.

[7] J. De Smet, P. Gzil, N. Vervoort, H. Verelst, G. Baron, G. Desmet, Influence of the pillar shape on the band broadening and the separation impedance of perfectly ordered 2-d porous chromatographic media, Anal. Chem. 76 (2004) 3716.

[8] M. De Pra, W. De Malsche, G. Desmet, P. Schoenmakers, W. Kok, Pillar-structured microchannels for on-chip liquid chromatography: Evaluation of the permeability and separation performance, J. Sep. Sci. 30 (2004) 1453.

[9] S. Umeda, S. Torii, Numerical and experimental study on thermal fuild flow over twin diamond-shaped cylinders in free stream, 15th International Symposium on Flow Visualization, Minsk, Belarus, June 25-28.

[10] S. Torii, S. Umeda, Flip-flop flow control inside streamwise diverging diamond-shaped cylinder bundles with concavities, Journal of Flow Control, Measurement and Visualization 1 (2013) 77–85.

[11] S. Hirasawa, A. Fujiwara, T. Kawanami, K. Shirai, Forced convection heat transfer coefficient and pressure drop of diamond-shaped fin-array, Journal of Electronics Cooling and Thermal Control 4 (2014) 78–85.

[12] S. Rashidi, M. Bovand, I. Pop, M. Valipour, Numerical simulation of forced convective heat transfer past a square diamond-shaped porous cylinder, Transp Porous Med 102 (2014) 207–225.

[13] S. Rashidi, R. Massodi, M. Bovand, M. Valipour, Numerical study of flow around and through a porous diamond cylinder in different apex angles, International Journal of Numerical Methods for Heat and Fluid Flow 24 (2014) 1504–1518.

[14] M. Valipour, S. Rashidi, M. Bovand, R. Massodi, Numerical modeling of flow around and through a porous cylinder with diamond cross section, European Journal of Mechanics - B/Fluids 46 (2014) 74–81.

[15] T. Vijaybabu, K. Anirudh, S. Dhinakaran, LBM simulation of unsteady flow and heat transfer from a diamond-shaped porous cylinder, International Journal of Heat and Mass Transfer 120 (2018) 267–283.

[16] R. Hilpert, Warmeabgage von geheizten drahten und rohren im luftstrom, ForshArb. Ing. Wes. 4 (1933) 215.

[17] W. McAdams, Heat transmission, third edition, chap. x, McGraw-Hill Book Co. Inc.

[18] D. Tritton, Experiments on the flow past a circular cylinder at low reynolds numbers, J. Fluid Mechanics 6, 547-567.

[19] M. Collis, D.C. Williams, Two-dimensional convection from heated wires at low reynolds number, Aeronautical research laboratories, Australian defence scientific service.

[20] C. Dennis, G. Chang, Numerical solutions for steady flow past a circular cylinder at reynolds numbers up to 100, J. Fluid Mech. 42 (1970) 471–489.

[21] B. Fornberg, A numerical study of steady viscous flow past a circular cylinder, Fluid Mechanics, vol.98, part 4, pp. 819-855.

[22] G. Sheard, K. Hourigan, M. Thompson, Computations of the drag coefficients for low-reynolds-number flow past rings, J. Fluid Mech. 526 (2005) 257–275.

[23] J. Kalita, R. Ray, A transformation-free hoc scheme for incompressible viscous flows past an impulsively started circular cylinder, Journal of Computational Physics 228 (2009) 5207–5236.

[24] A. Okajima, Strouhal numbers of rectangular cylinders, J Fluid Mech 123 (1982) 379.

[25] M. Breuer, J. Bernsdorf, T. Zeiser, F. Durst, Accurate computations of the laminar flow past a square cylinder based on two different methods: lattice-boltzmann and finite-volume, Int. J. Heat Fluid Flow 21 (2000) 186–196.

[26] A. Sharma, W. Eswaran, Heat and fluid flow across a square cylinder in the two-dimensional laminar flow regime, Numerical Heat Transfer, Part A: Applications 45 (2004) 247–269.

[27] A. Dhiman, R. Chhabra, W. Eswaran, Flow and heat transfer across a confined square cylinder in the steady flow regime: Effect of peclet number, International Journal of Heat and Mass Transfer 48 (2005) 4598–4614.

[28] A. Sahu, R. Chhabra, W. Eswaran, Effects of reynolds and prandtl numbers on heat transfer from a square cylinder in the unsteady flow regime, International Journal of Heat and Mass Transfer 52 (2009) 839–850.

[29] D. Yoon, K. Yang, C. Choi, Flow past a square cylinder with an angle of incidence, Physics of FLuids 22 (2010) 043603.

[30] S. Djeddi, A. Masoudi, P. Ghadimi, Numerical simulation of flow around diamond-shaped obstacles at low to moderate reynolds numbers, American Journal of Applied Mathematics and Statistics 1 (2013) 11–20.

[31] C. Dalton, W. Zheng, Numerical solutions of a viscous uniform approachflow past square and diamond cylinders, Journal of Fluids and Structures 18 (2003) 455–465.

[32] Z. Li, J. Davidson, S. Mantell, Numerical simulation of flow field and heat transfer of streamlined cylinders in cross flow, Journal of Heat Transfer 128 (2006) 564–570.

[33] N. Delany, N. Sorensen, Low-speed drag of cylinders of various shapes., NACA technical note 3038.

[34] H. Weller, G. Tabor, H. Jasak, C. Fureby, A tensorial approach to computational continuum mechanics using object-oriented techniques, Computers in physics 12 (1998) 620.

[35] J. Magnaudet, M. Rivero, J. Fabre, Accelerated flows past a rigid sphere or a spherical bubble. part 1: Steady straining flow, Journal of Fluids Mechanics 284 (1995) 97–135.

[36] A. Dani, A. Cockx, P. Guiraud, Direct Numerical Simulation of Mass Transfer from Spherical Bubbles: the Effect of Interface Contamination at Low Reynolds Numbers, International Journal of Chemical Reactor Engineering 4 (2006) 1.

[37] Z. Huang, D. Legendre, P. Guiraud, Effect of interface contamination on particle-bubble collision, Chemical Engineering Science 68 (2012) 1–18.

[38] J. Leontini, D. Lo Jacono, M. Thompson, Stability analysis of the elliptic cylinder wake, Journal of Fluid Mechanics 763 (2015) 302–321.

[39] C. Jackson, A finite-element study of the onset of vortex shedding in flow past variously shaped bodies, Journal of Fluid Mechanics 182 (1987) 23–45.

[40] S. Dhinakaran, J. Ponmozhi, Heat transfer from a permeable square cylinder to a flowing fluid, Energy conservation and management 52 (2011) 2170–2182.

[41] I. Morenko, V. Fedyaev, E. Galimov, Cross-flow and heat transfer of porous permeable cylinder, IOP Conf. Series: Materials Science and Engineering 86 (2015) 012012.

[42] R. Bird, W. Stewart, E. Lightfood, Transport phenomena, 2nd ed., John Wiley and sons, inc (2002).

[43] D. Colombet, D. Legendre, A. Cockx, P. Guiraud, Mass or heat transfer inside a spherical gas bubble at low to moderate reynolds number, International Journal of Heat and Mass Transfer 67 (2013) 1096–1105.

[44] D. Legendre, On the relation between the drag and the vorticity produced on a clean bubble, Physics of Fluids 19 (2007) 018102.

Nomenclature

Roman symbols

a	diamond-shaped cylinder width m
b	diamond-shaped cylinder length, m
C_p	heat capacity at constant pressure, $\mathrm{J\,kg^{-1}\,K^{-1}}$
C_D	drag coefficient
D_T	~~heat~~ thermal diffusivity ($D_T = \lambda/(\rho C_p)$), $\mathrm{m^2\,s^{-1}}$
h	heat transfer coefficient, $\mathrm{W\,m^{-2}\,K^{-1}}$
H	cylinder length, m
J	surface averaged heat flux, $\mathrm{W\,m^{-2}}$
J_{Loc}	local average heat flux, $\mathrm{W\,m^{-2}}$
L_{ref}	reference length (D or a), m
Nu	Nusselt number based on the cylinder width (D or a)
p	local pressure, Pa
Pr	Prandtl number, $Pr = \nu/D_T$
Re	Reynolds number based on the cylinder width (D or a) and far field velocity U
Re'	Reynolds number based on the cylinder width (D or a) and velocity scale U'
Re_{crit}	Reynolds number corresponding to the onset on the recirculation formation
Re'_{crit}	Estimation of the Reynolds number corresponding to an unsteady oscillatory flow
T	local temperature, K
T_p	temperature imposed at wall, K
T_∞	inlet (or far field) temperature, K
t	time, s
u	local velocity, $\mathrm{m\,s^{-1}}$
U	inlet (or far field) velocity, $\mathrm{m\,s^{-1}}$
U'	reference velocity based on the maximal vorticity magnitude ($U' = \Omega_{max} a/2$), $\mathrm{m\,s^{-1}}$

Greek symbols

α	apex angle of the diamond-shaped cylinder, $^\circ$
δ_T	mean thickness of the thermal boundary layer around the cylinder, m
λ	thermal conductivity of phase k, $\mathrm{W\,m^{-1}\,K^{-1}}$
μ	dynamic viscosity, Pa s
ν	kinematic viscosity ($\nu = \mu/\rho$), $\mathrm{m^2\,s^{-1}}$
ω	vorticity, $\mathrm{s^{-1}}$
Ω_{max}	maximal vorticity magnitude near the equator angle, $\mathrm{s^{-1}}$
ρ	density, $\mathrm{kg\,m^{-3}}$
θ	angular position, $^\circ$

Mathematical symbol

$\|\| - \|\|$	vector magnitude

α [°]	grid	$Nb.L_A/sf$	$Nb.L_B/sf$	$Nb.L_C/sf$	$Nb.L_D/sf$	L_D/a	Total Nb
33	A	260/20	240/20	120/1	260/20	80	163 800
33	B	200/20	150/20	80/1	150/20	80	76 000
33	C	100/20	75/20	40/1	75/20	80	19 000
33	D	65/20	50/20	20/1	50/20	80	7 800
50	B	200/20	150/10	60/1	150/13	60	72 000
60	B	200/20	150/10	60/1	150/12.5	80	72 000
90	A	250/20	150/20	70/1	240/20	100	115 000
90	B	200/20	120/20	50/1	200/20	100	74 000
90	C	100/20	60/20	24/1	100/20	100	18 400
90	D	50/20	30/20	12/1	50/20	100	4 600
120	B	200/20	150/10	40/1	150/20	100	68 000

Table 1: Computational domain and grid dimensions for the case of the diamond-shaped cylinder, grid B is the mesh used for the main simulations (segments A B C D, $L_A/a = L_B/a = 60$, sf= scale factor between the largest and smallest cell length).

α [°]	Re	$grid$	C_D	ER [%]	Nu	ER [%]
33	100	A	0.9459	0.31	3.1994	0.01
33	100	B	0.9488	-	3.1990	-
33	100	C	0.9595	1.13	3.2024	0.11
33	100	D	0.9878	4.11	3.2109	0.37
90	40	A	1.5686	0.92	3.2355	0.02
90	40	B	1.5833	-	3.2361	-
90	40	C	1.6290	2.89	3.2547	0.57
90	40	D	1.7092	7.96	3.3223	2.66

Table 2: Tests of grid refinement independence on drag coefficient and Nusselt number; ER is the relative difference between the obtained value with the mesh used for simulations (mesh B).

Re	C_D^a	C_D^b	C_D^c	C_D^d	C_D^e	Nu^f	Nu^g	Nu^h	Nu^e
1	-	-	11.775	-	11.240	0.891	0.750	0.800	0.816
2	-	-	7.259	-	7.041	-	-	-	-
3	-	-	-	-	5.476	-	-	-	-
4	-	-	-	-	4.624	-	-	-	-
5	4.116	-	-	-	4.157	1.525	1.313	1.395	1.418
6	-	-	-	-	3.689	-	-	-	-
7	3.421	-	-	-	3.459	-	-	-	-
8	-	-	-	-	3.170	-	-	-	-
9	-	-	-	-	2.985	-	-	-	-
10	2.846	-	2.854	-	2.833	1.992	1.744	1.818	1.855
15	-	-	-	-	2.329	2.328	2.078	2.134	2.181
20	2.045	2.001	2.072	2.019	2.043	2.602	2.362	2.396	2.446
25	-	-	-	-	1.854	2.835	2.613	2.624	2.683
30	-	-	-	-	1.716	3.041	2.841	2.828	2.892
35	-	-	-	-	1.610	3.227	3.051	3.013	3.082
40	1.522	1.498	1.545	1.514	1.526	3.397	3.248	3.185	3.256

Table 3: Drag coefficient and Nusselt number for a cylinder: previous works of (a) Dennis & Chang [20], (b) Fornberg [21], (c) Sheard et al. 2005 [22] (Digitized data of Fig. 6 in the article), (d) Kalita & Ray [23], (e) this work, (f) Hilpert 1933 [16], (g) Mcadams 1954 [17], (h) Collis & Williams 1969 [19].

α	Re_{crit}	A	B	Re'_{crit}
30	55.0	0.0541	-2.9815	-
33	46.6	0.0604	-2.8187	130(120)
35	41.8	0.0665	-2.7808	-
40	33.2	0.0788	-2.6168	-
50	23.0	0.1031	-2.3711	75(60)
60	17.4	0.1154	-2.0051	-
90	7.4	0.1824	-1.3598	50(40)
120	3-4	0.2353	-0.7598	-
circular cylinder	6.24	0.1324	-0.8265	45(40)

Table 4: Estimation of the critical Reynolds number Re_{crit} corresponding to the onset of the recirculation behind the cylinder and constants used in Eq. 10 for the prediction of this recirculation wake length, Re'_{crit} Reynolds number corresponding to an unsteady oscillatory flow: the first value corresponds to the observation of oscillations on the lift coefficient and the value in parenthesis for which the flow is found to remain steady.

α	A	n
33	0.829	0.453
40	1.080	0.435
50	1.483	0.427
60	1.941	0.416
90	2.919	0.403
120	2.971	0.431
circular cylinder	0.950	0.490

Table 5: Constants of Eq. 11 for the estimation of maximal vorticity intensity.

α	A	B	n
30	6.6800	0.9482	0.5702
33	6.7648	0.8763	0.5827
35	6.7010	0.8721	0.5872
40	6.5646	0.8443	0.6002
50	6.9266	0.6907	0.6397
60	7.1043	0.6089	0.6717
90	6.9857	0.5651	0.7201
120	6.8338	0.5886	0.7392

Table 6: Constants of Eq. 12 for the estimation of the drag coefficient.

Re	(a)	(b)	(c)
5	1.459	1.49038 (2.1%)	1.49696 (2.6%)
10	1.888	1.85577 (1.7%)	1.91962 (1.7%)
20	2.460	2.47115 (0.4%)	2.49371 (1.4%)
30	2.880	2.91346 (1.1%)	2.92318 (1.5%)
40	3.236	3.25962 (0.7%)	3.28956 (1.7%)

Table 7: Nusselt numbers comparison for the case $\alpha = 90°$: (a) this work, (b) Rashidi et al.[12] (relative difference), (c) Vijaybabu et al. [15] (relative difference).

α	A	B
33	0.179	0.309
40	0.209	0.340
50	0.264	0.371
60	0.319	0.397
90	0.456	0.445
120	0.5638	0.4626

Table 8: Constants for Nusselt number estimation from Eq. 13.

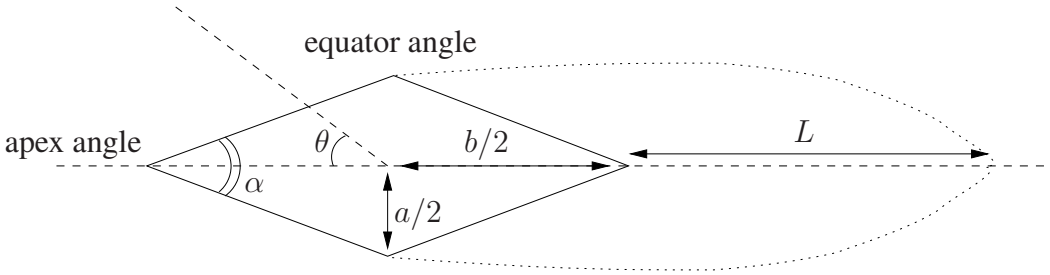

Figure 1: Diamond-shaped cylinder geometry: 'a' cylinder section width, 'b' cylinder section length, α apex angle value, θ angular position, 'L' wake length definition ($\alpha = 2\times\arctan(a/b)$).

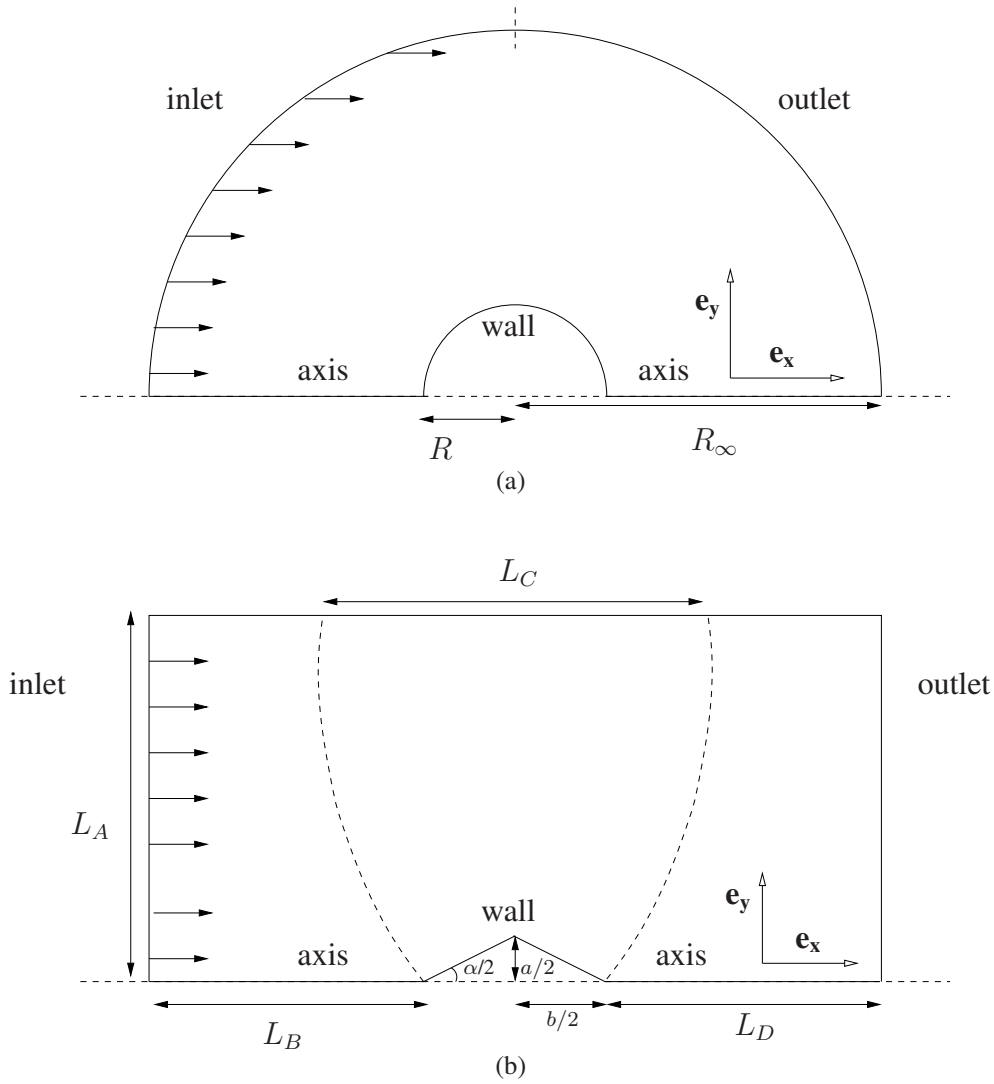

Figure 2: (a) Computational domain (a) for a cylinder and (b) for a diamond-shaped cylinder.

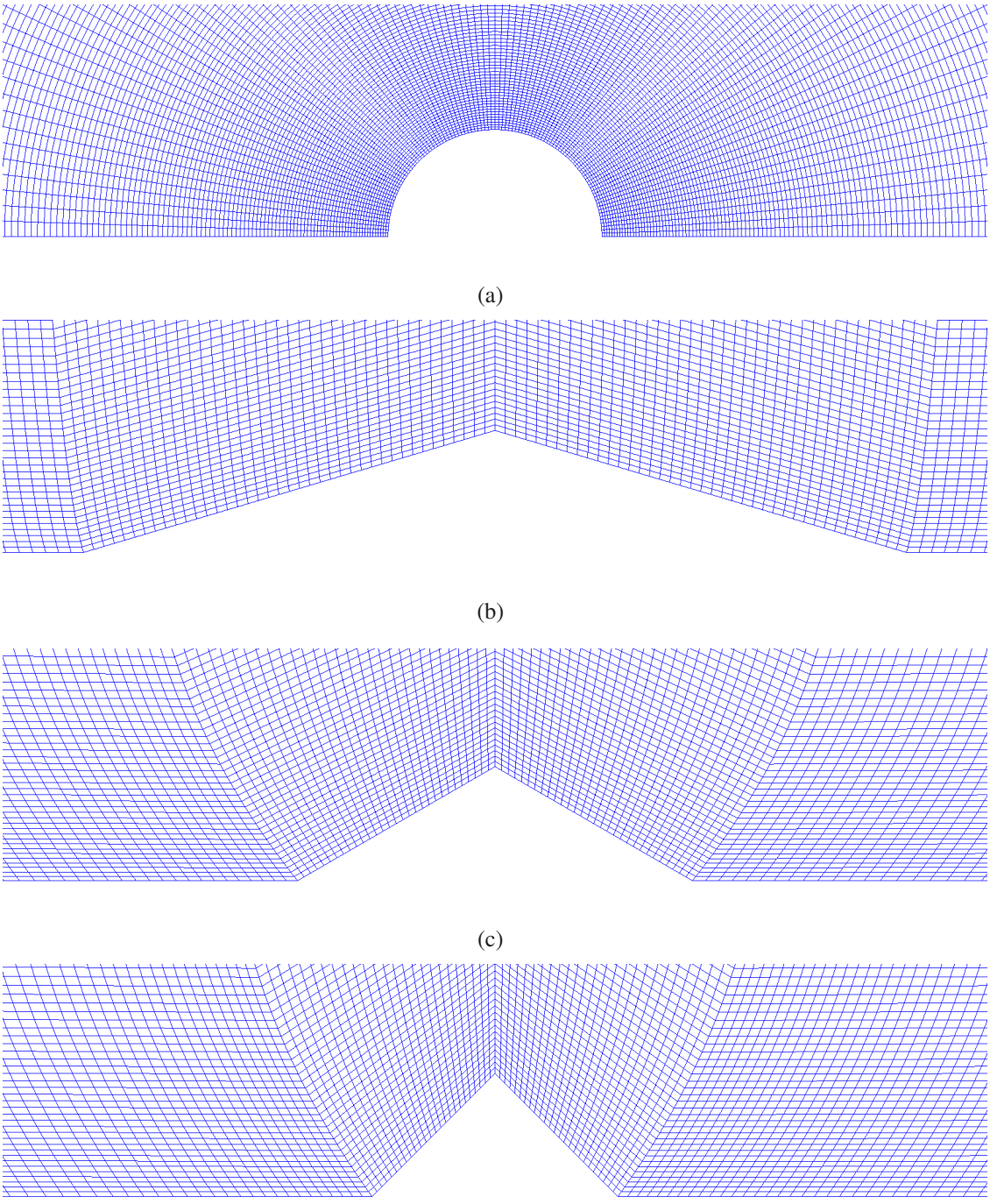

Figure 3: Zoom around the cylinder mesh for the (a) circular cylinder and the diamond-shaped cylinder with the mesh B for (b) $\alpha = 33°$, (c) $\alpha = 60°$ and (d) $\alpha = 90°$.

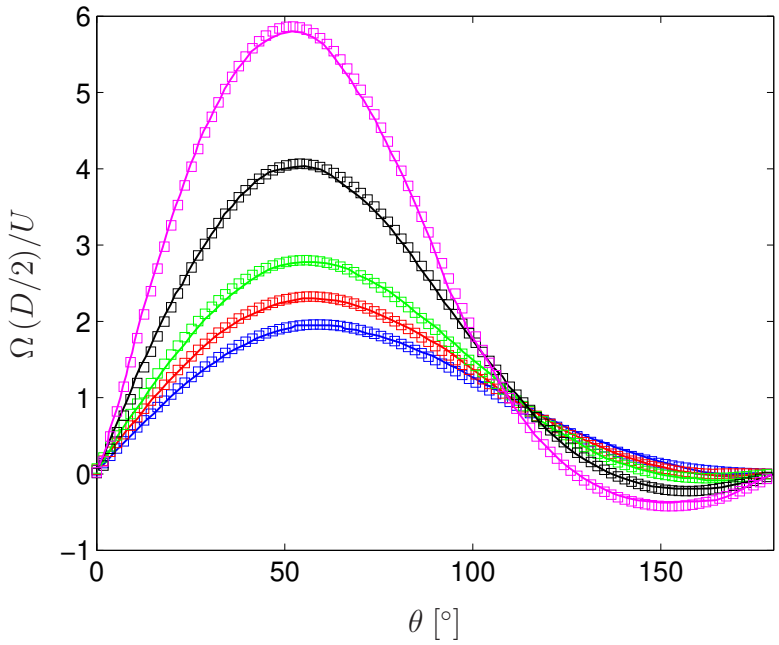

Figure 4: Vorticity along a circular cylinder surface as a function of the angular position with from top to the bottom $Re = 5 - 7 - 10 - 20 - 40$; lines : numerical simulation of Dennis & Chang [20], symbols : this work ($\theta = 0$ and $\theta = 180^\circ$ correspond respectively to the stagnation points at the front and back of the cylinder).

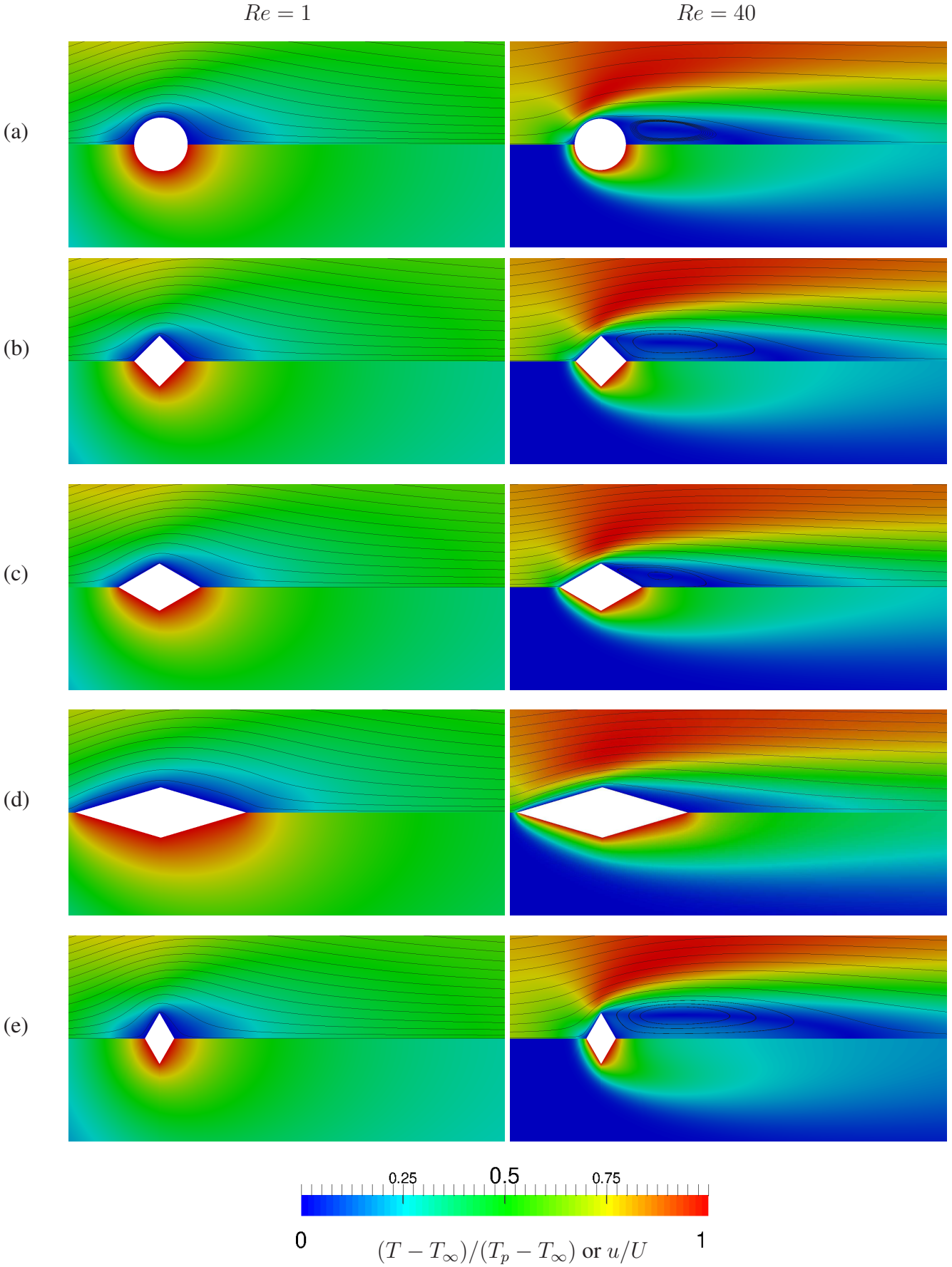

Figure 5: Velocity field with streamlines (top part) and temperature field (bottom part) for the steady state flow and heat transfer around a cylinder for (a) a circular cylinder and a diamond-shaped cylinder with (b) $\alpha = 90°$, (c) $\alpha = 60°$, (d) $\alpha = 33°$ and (e) $\alpha = 120°$.

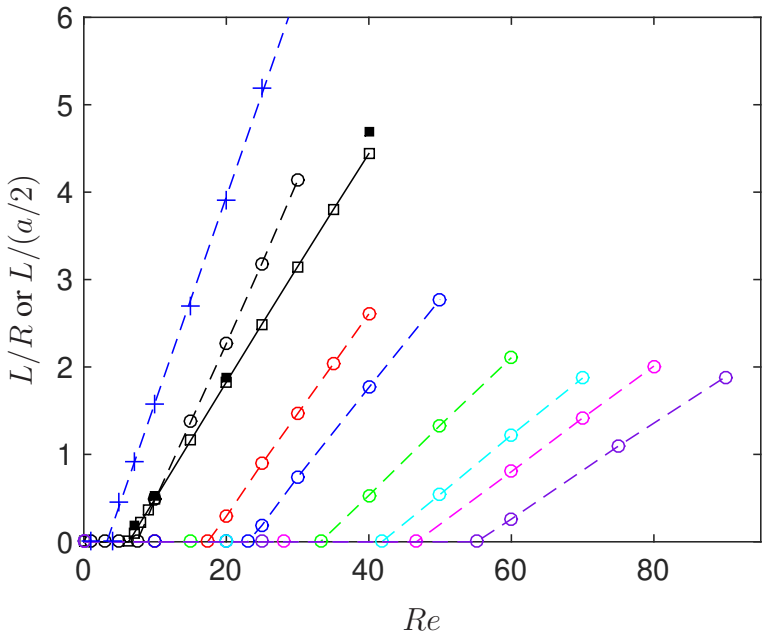

Figure 6: Dimensionless wake length as a function of the Reynolds number Re: diamond-shaped cylinder with $\alpha =$ $\circ$ 30°, $\circ$ 33°, $\circ$ 35°, $\circ$ 40°, $\circ$ 50°, $\circ$ 60°, $\circ$ 90°, $+$ 120°; $--$ Eq. 10; circular cylinder from $\square$ this work and according to $\blacksquare$ Dennis & Chang [20].

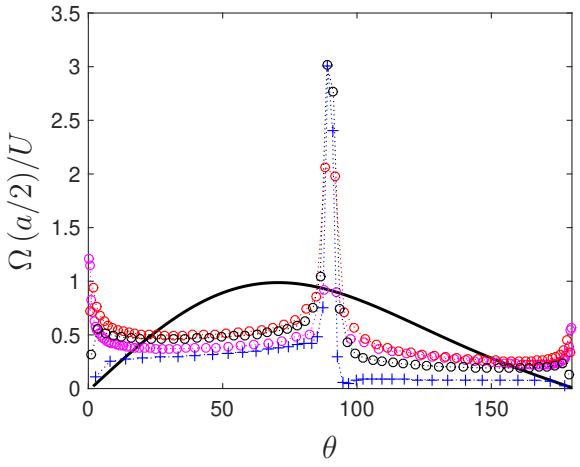

(a)

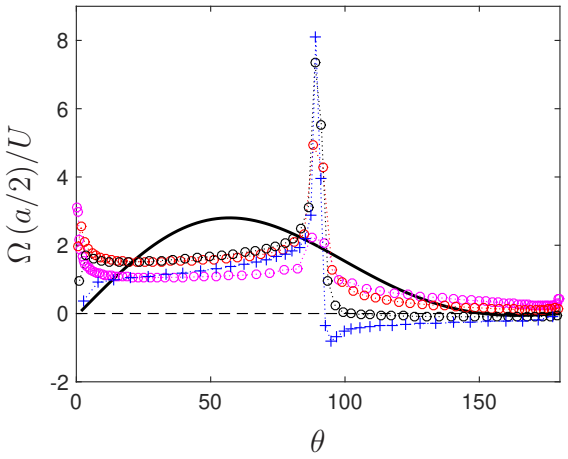

(b)

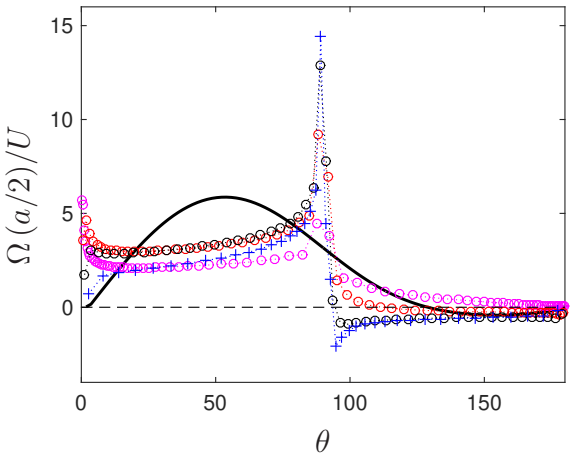

(c)

Figure 7: Vorticity at the cylinder surface as a function of the angular position θ for (a) $Re = 1$, (b) $Re = 10$, (c) $Re = 40$: diamond-shaped cylinder with $\alpha = \circ$ 33°, $\circ$ 60°, $\circ$ 90°, $+$ 120° and – circular cylinder.

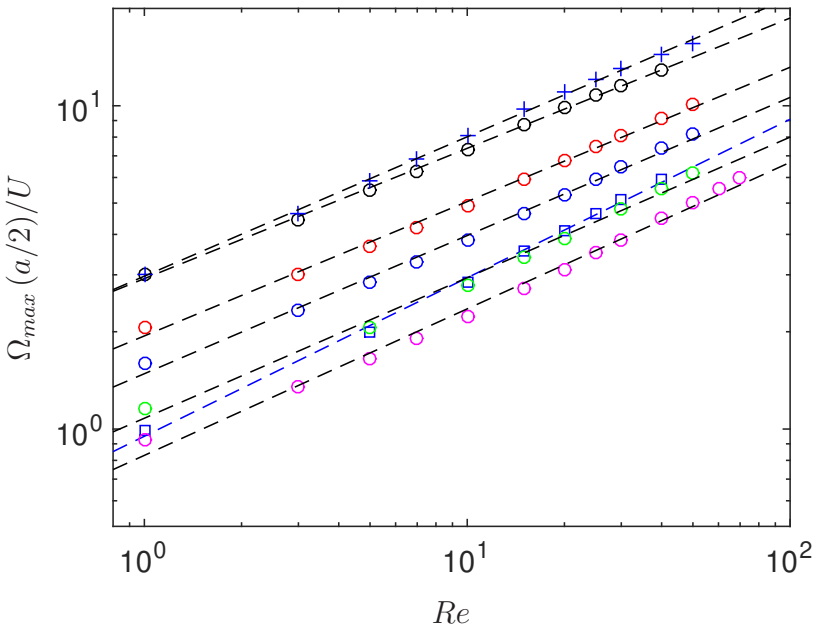

Figure 8: Maximal vorticity magnitude near the equator angle as a function of the Reynolds number : diamond-shaped cylinder with $\alpha = \circ$ 33°, $\circ$ 40°, $\circ$ 50°, $\circ$ 60°, $\circ$ 90°, $+$ 120°; $\square$ circular cylinder (for this case the maximal vorticity is not systemically at the equator, see Fig. 4); $--$ Eq. 11.

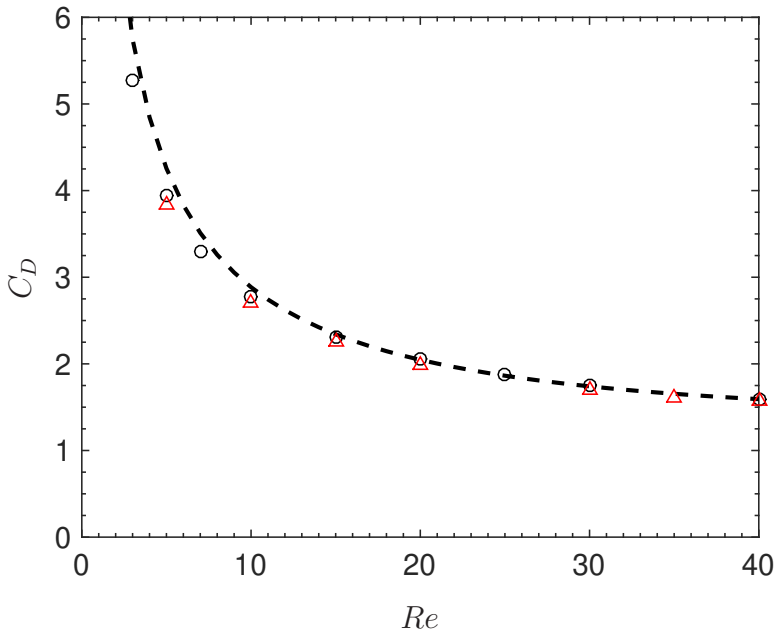

Figure 9: Drag coefficient as a function of the Reynolds number for a diamond-shaped cylinder with $\alpha = 90°$: △, Yoon et al. [29] ∘ this work and $--$ for a circular cylinder.

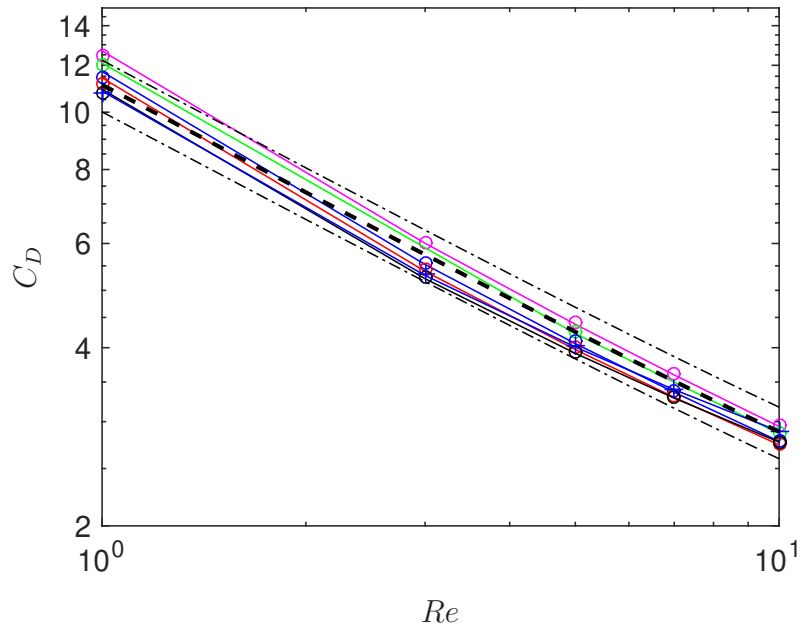

(a)

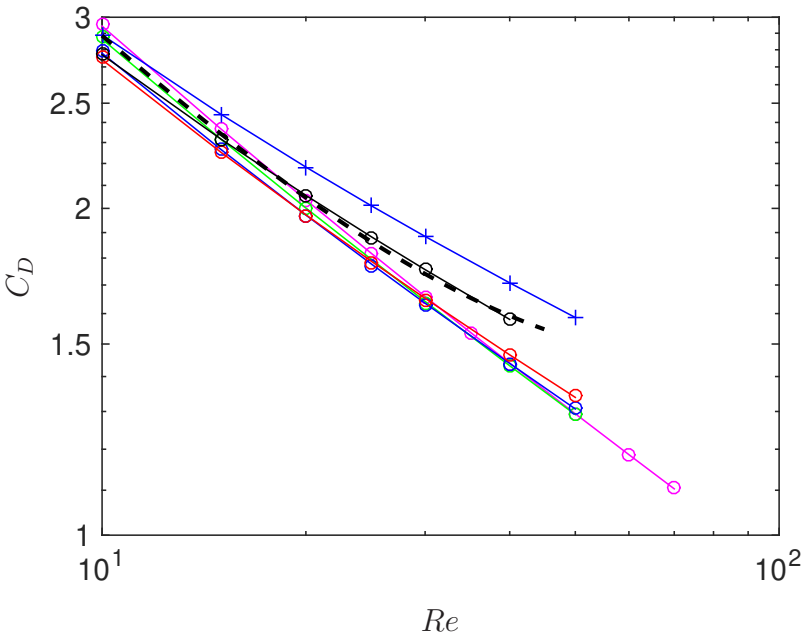

(b)

Figure 10: Drag coefficient as a function of the Reynolds number for (a) $1 \leq Re \leq 10$ and (b) $10 \leq Re \leq 70$: diamond-shaped cylinder with $\alpha = \circ$ 33°, $\circ$ 40°, $\circ$ 50°, $\circ$ 60°, $\circ$ 90°, $+$ 120°; lines : Eq. 12; $--$ circular cylinder and $-.-$ $\pm 10\%$ of circular cylinder drag coefficient.

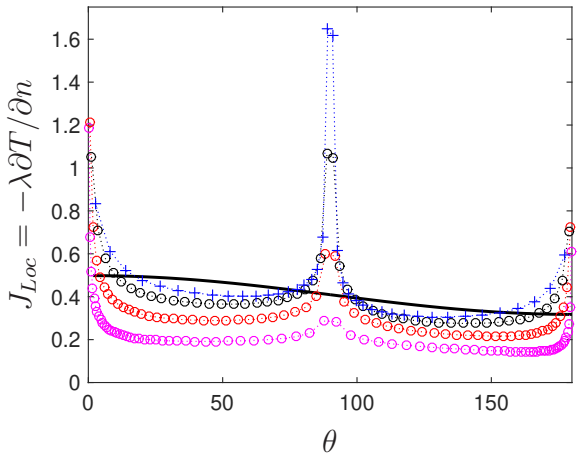

(a)

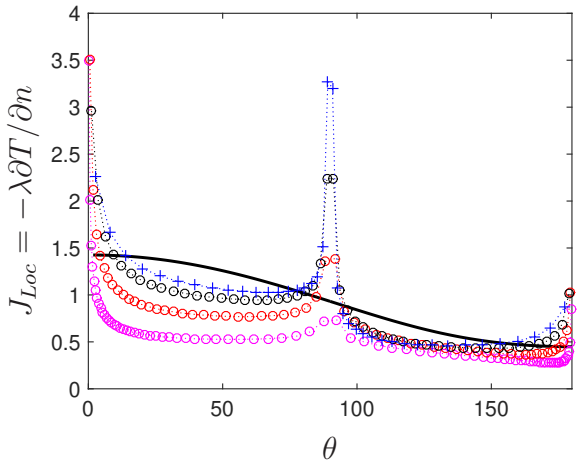

(b)

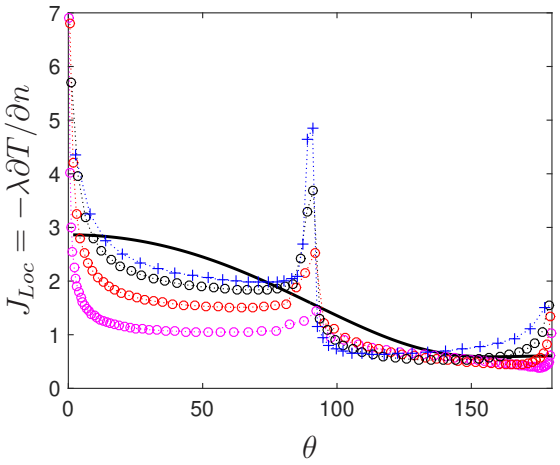

(c)

Figure 11: Local heat flux as a function of the angular position θ for (a) $Re = 1$, (b) $Re = 10$, (c) $Re = 40$: – circular cylinder and diamond-shaped cylinder with $\alpha = \circ$ 33°, $\circ$ 60°, $\circ$ 90°, $+$ 120°.

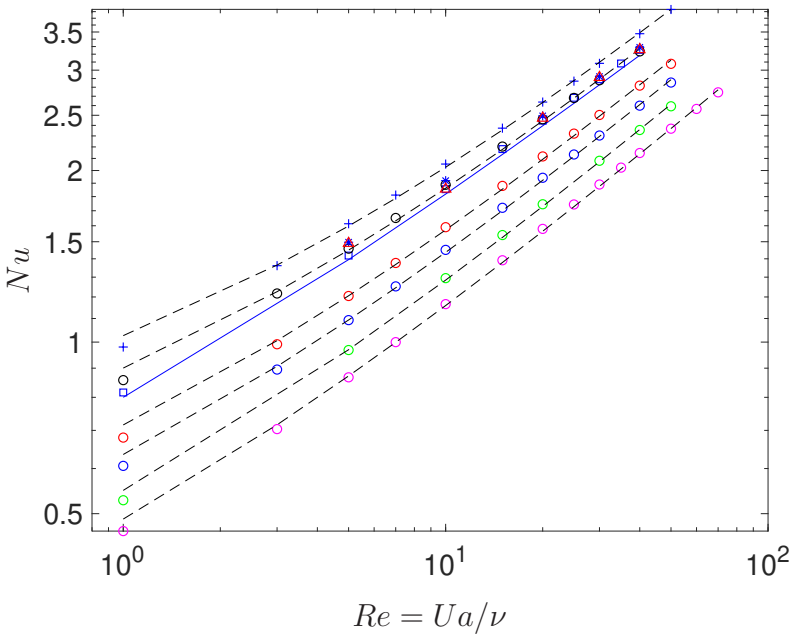

Figure 12: Nusselt number as a function of the Reynolds number;□ circular cylinder and — Eq. 9; diamond-shaped cylinder with $\alpha =$ ○ 33°, ○ 40°, ○ 50°, ○ 60°, ○ 90°, + 120°; diamond-shaped cylinder with $\alpha = 90°$ according to △ Rashidi et al.[12] and * Vijaybabu et al. [15] ; −− Eq.13.

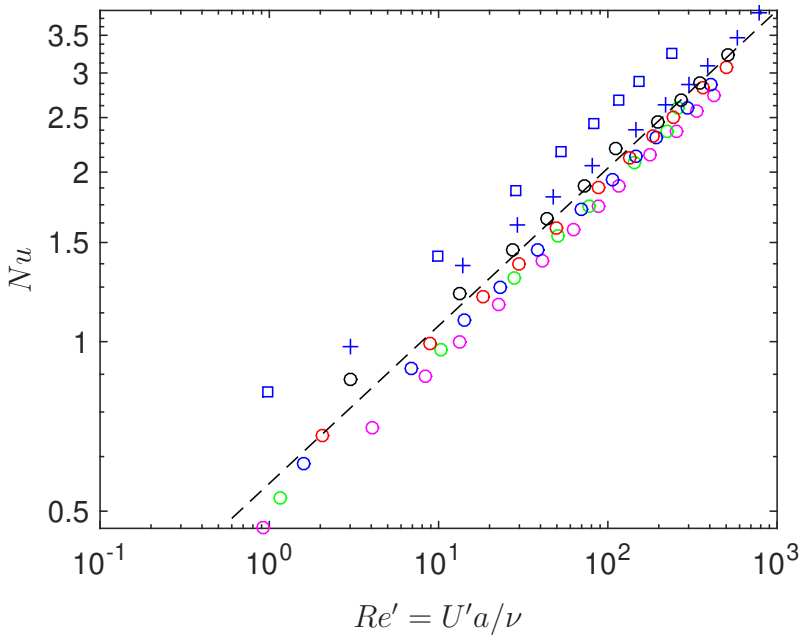

Figure 13: Nusselt number as a function of the Reynolds number $Re = U'a/\nu$ with $U' = \Omega_{max}(a/2)$: diamond-shaped cylinder with $\alpha =$ ○ 33°, ○ 40°, ○ 50°, ○ 60°, ○ 90°, + 120°; □ circular cylinder; $---$ $Nu = 0.56\, Re'^{0.28}$.